Electronic Supplementary Material (ESI) for Materials Advances.

Supporting Information for

Do partially filled degenerate orbitals exhibit crystal anisotropy?

Taishun Manjo, Shunsuke Kitou, Naoyuki Katayama, Shin Nakamura, Takuro Katsufuji, Yoichi Nii, Taka-hisa Arima, Joji Nasu, Takumi Hasegawa, Kunihisa Sugimoto, Daisuke Ishikawa, Alfred Q. R. Baron, and Hiroshi Sawa*

Correspondence to: z47827a@cc.nagoya-u.ac.jp

Contents

1. Synthesis and X-ray diffraction experiment

Single crystals of FeV_2O_4 were grown by the floating–zone method in Ar gas flow.

X-ray diffraction (XRD) experiments using single crystals were performed on the BL02B1 beamline at the synchrotron facility SPring-8 in Japan. XRD data were obtained at $T = 160\ K$ (cubic phase). A Pilatus3 X 1M CdTe detector was used. The incident energy of the synchrotron X-rays was $E = 40\ keV$. The XRD measurements were completed in approximately 1 h. For crystal structural analysis, diffraction intensity averaging was performed using SORTAV[1]. The crystal structure and electron density (ED) analyses were performed using JANA2006[2]. The crystal structure and ED distribution were visualized using VESTA[3]. Our crystal structural parameters are consistent with those of previous reports[16] (Tables S1 and S2). The high-angle analysis was performed with the data in the range of $0.83\ \text{Å}^{-1} \leq \sin\theta/\lambda \leq 1.79\ \text{Å}^{-1}$ to determine the core term precisely for the CDFS method (Fig. S1).

2. VED simulation

The following formulae describe the three t_{2g} orbital wave functions of V with the <1 1 1> direction as the quantum axis:

$$\begin{cases} \varphi_1(r) = \frac{1}{\sqrt{3}}(|yz\rangle + |zx\rangle + |xy\rangle) \\ \varphi_2(r) = \frac{1}{\sqrt{2}}(|yz\rangle - |zx\rangle) \\ \varphi_3(r) = \frac{1}{\sqrt{6}}(|yz\rangle + |zx\rangle - 2|xy\rangle) \end{cases} \#(S1)$$

In these formulae, x,y,z are parallel to the lattice vectors a,b,c.

We assume that the orbital state is calculated using a point-charge model with the Ewald method [30]. As described in the main text, one electron occupies the lower φ_1, and the other is lifted to the degenerate orbitals and occupies either φ_2 or φ_3. This electron configuration satisfies $S = 1$. It is not clear whether the lifted electron occupies φ_2 or φ_3. When only φ_2 is occupied, the VED is described as $|\varphi_1|^2 + |\varphi_2|^2$ (Fig. S2A). Although it is similar to the

observed VED, the shape of the ring-like component cannot be reproduced. Similarly, we assume that the lifted electron occupying φ_3 cannot reproduce the experimental results (Fig. S2B).

3. Structural analysis and the CDFS analysis of the high-temperature tetragonal phase

In the high-temperature tetragonal phase in FeV_2O_4, non-merohedral domain structures are formed in the crystal owing to reduced symmetry. Three domains with different crystal orientations were formed in the structural phase transition from cubic to tetragonal. However, because the crystal used in our XRD experiment had only two domains, the crystal structural analysis was performed using the twin law, which is expressed as follows:

$$\begin{pmatrix} h \\ k \\ l \end{pmatrix}_{domain2} = \begin{pmatrix} 0.5 & -0.5 & 0.5 \\ -0.5 & 0.5 & 0.5 \\ -1 & -1 & 0 \end{pmatrix} \begin{pmatrix} h \\ k \\ l \end{pmatrix}_{domain1} \#(S2)$$

Although the diffraction peaks associated with this matrix did not overlap in reciprocal space, the intensities of these peaks were merged as pseudo–merohedral. Tables S3 and S4 list the results of the analysis using the twin law. The domain ratio was $domain1 : domain2 = 0.660(8) : 0.340$. The FeO_4 tetrahedron was compressed in the *c*-axis direction (Fig. S4).

The CDFS analysis was performed using the structural parameters obtained from the pseudo–merohedral analysis. Consequently, the VED at the Fe site had an anisotropic shape, similar to the $|3z^2 - r^2\rangle$ orbital (Fig. S4). In contrast, the anisotropy of the VED at the V site exhibited little change (Fig. S5). Note that this analysis included the effects of the domains.

4. First-principles calculation of phonon modes

The first-principles calculations of the phonon modes in FeV_2O_4 in the cubic phase were performed using the ABINIT package[4] with the local spin density approximation (LSDA) parametrized by Perdew and Wang[5], and the projector augmented wave method. The partial waves and projector functions were generated by ATOMPAW[6] with valence configurations of

$3s^2\,3p^6\,3d^6\,4s^2$ for Fe, $3s^2\,3p^6\,3d^2\,4s^2\,4p^1$ for V, and $2s^2\,2p^4$ for O. The plane wave cutoff energy was 544 eV, and the k point mesh on the 4 × 4 × 4 Monkhorst–Pack grid in the cubic phase Brillouin zone was used. The crystal structure is taken from the observed one, which is shown in Tables S1 and S2.

The phonon calculations should be performed with an electronic state close to the observed state. We examined the LSDA+U method[7] in the full localized limit formalism (Eq. (4) of Ref. 7). When U = 0.0 eV, the obtained electronic state is a ferrimagnetic metallic state with a small total magnetic moment M = 0.15 $\mu_B/f.u.$. For $U \geq$ 1.0 eV, the total magnetic moment becomes 0. This state is half-metallic, where Fe 3*d* bands with up-spin are fully occupied and the down-spin bands of Fe and V are partially filled. This electronic state is preferable because only the down-spin bands are metallic. If we increase U above 3.0 eV, the electronic state of V changes from $a_{1g}^1\,e_g^1$ to e_g^2, where a_{1g} is φ_1 and e_g corresponds to φ_2 and φ_3 in the main text. Since the observed state of V is $a_{1g}^1\,e_g^1$, we choose U = 2.0 eV. Independent of U, the electronic state is metallic, because U does not break the degeneracy of e_g orbitals of Fe and V. The Fermi Dirac distribution with T = 27.2 meV was applied, as the calculated electronic state is metallic. The interatomic force constants were obtained via the frozen phonon method with $1 \times 1 \times 1$ primitive unit cell. The phonon modes are calculated from those interatomic force constants. The inelastic X-ray scattering (IXS) spectra are estimated according to Ref. 8.

From the calculation result, the E_u longitudinal optical (LO) mode is observed in the $[0\ 0\ 1]$ direction from $(0\ 0\ 8)$ in the reciprocal space (Fig. S7A). The E_g transverse acoustic (TA) mode is observed in the $[\bar{1}\ 1\ 0]$ direction from $(8\ 8\ 0)$ in the reciprocal space (Fig. S8A). These two modes were observed in the IXS experiment.

5. IXS experiment

IXS experiments were performed on the RIKEN BL43LXU beamline at the synchrotron facility SPring-8 in Japan. A Si $(11\ 11\ 11)$ backscattering setup with an energy resolution of 1.5 meV and an incident X-ray energy of 21.747 keV was chosen. Because the linear absorption coefficient of FeV_2O_4 at this energy is as high as $58.74\ cm^{-1}$, the measurement was performed

under reflection conditions. Two samples were prepared to perform measurements in two directions: the [0 0 1] and [$\bar{1}$ 1 0] directions. They were mounted on the same sample holder in a closed-cycle cryostat, and the measurements for each direction were performed under the same conditions. A 2D analyzer array was used in the experiments.

6. IXS experimental result and discussion

Fig. S7B shows the 2D colormaps of the energy spectra obtained from IXS experiments. The 2D colormaps are qualitatively the same as calculation results. The experimental data were fitted by the convolution of the damping harmonic oscillator function with the Voigt function approximation of the instrumental resolution function. Figs. S8B and S9 show the dispersion obtained by fitting. The contribution to the phonon linewidth due to finite q-resolution was estimated at 0.15 meV. This value is small and does not affect the discussion in this paper.

As described in the main text and Fig. 5, the slight softening phonon indicates that the explosive development of the correlation length toward the transition temperature is suppressed because each FeO_4 tetrahedron is isolated by the surrounding VO_6 octahedrons, which have intrinsic orbital fluctuations in both the cubic state and high-temperature tetragonal phase. The behavior of the phonon is shown by the temperature dependence of the energy linewidth in Fig. S10. The linewidth of the phonons broadened toward the phase transition and then became narrower again after the phase transition. The inverse of the line width corresponds to the phonon lifetime, consistent with the temperature dependence of the softening.

The E_g-mode, which is a deformation distortion of the FeO_4 tetrahedron, also fluctuates in time and space (Fig. S6). When this orbital fluctuation and distortion mode are coupled, the degeneracy of the two orbitals can be solved. When the deformation modes of the FeO_4 tetrahedron are correlated between different sites, the energy gain component is generated by the alignment of the Fe orbitals in response to the lattice strain of E_g. In this case, the elastic stiffness constants decrease corresponding to the strain relaxation just above the transition temperature.

The elastic stiffness constant can be estimated from the slope of the dispersion of the acoustic modes at the lowest $\boldsymbol{q}$. The $\frac{C_{11}-C_{12}}{2}\left(=C^{'}\right)$ was estimated by dispersions of the E_g TA mode obtained by the IXS. Eq. (S3) was derived from *31*.

$$E(q)=\hbar|q|\sqrt{\frac{C^{'}}{\rho}}\#(S3)$$

Here, $\hbar$ is the Dirac constant, and ρ is the mass density of the unit cell. Calculations with the data at each temperature yielded $C^{'}_{300K}=17.6\ GPa$ and $C^{'}_{150K}=3.2\ GPa$, which are in good agreement with previously reported values[9]. The elastic stiffness constants just before the transition temperature decreased, indicating the occurrence of strain relaxation. The red and black dashed lines in Fig. 5D indicate the linear dispersions expected from the obtained elastic stiffness constants at 300 K and 150 K, respectively.

The behavior of the phonon energy linewidth and elastic stiffness constant also closely resembles the nematic state of iron-based superconductors, in which orbital degrees of freedom play an important role[31].

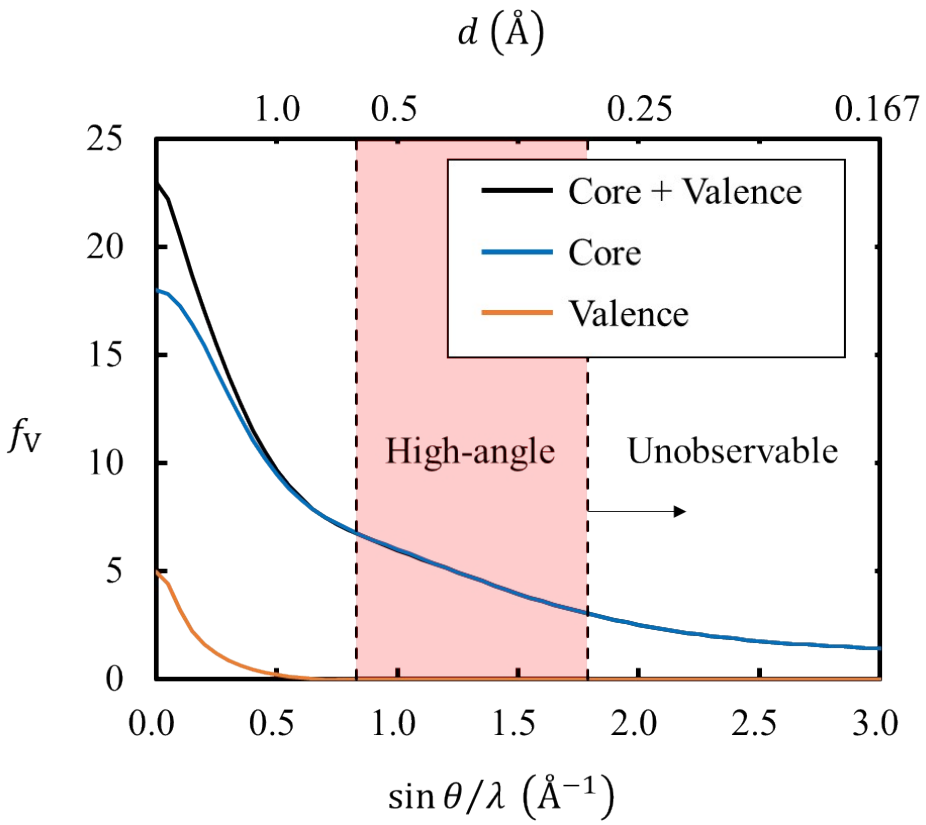

Fig. S1.

Atomic scattering factor of V [2]. Black, blue, and orange lines indicate the contribution of the total, core, and valence electrons, respectively.

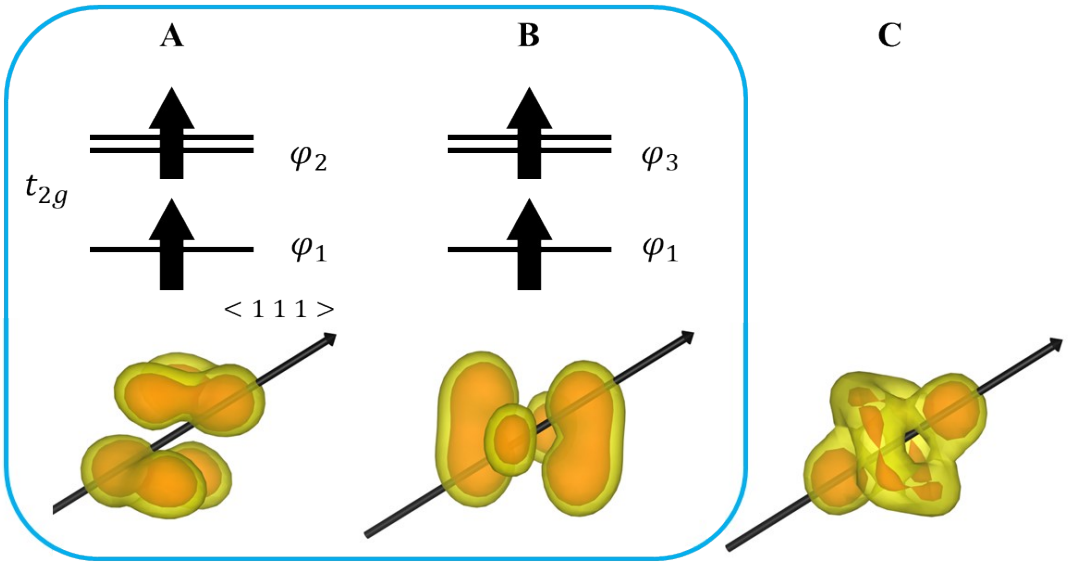

Fig. S2.

(**A**, **B**) Assumed electron configurations and simulated VED around V site. The red part of the VED highlights the characteristic components. (**C**) Observed VED around V (isosurface level 4.5e/Å^3 (yellow), 5.3e/Å^3 (red)).

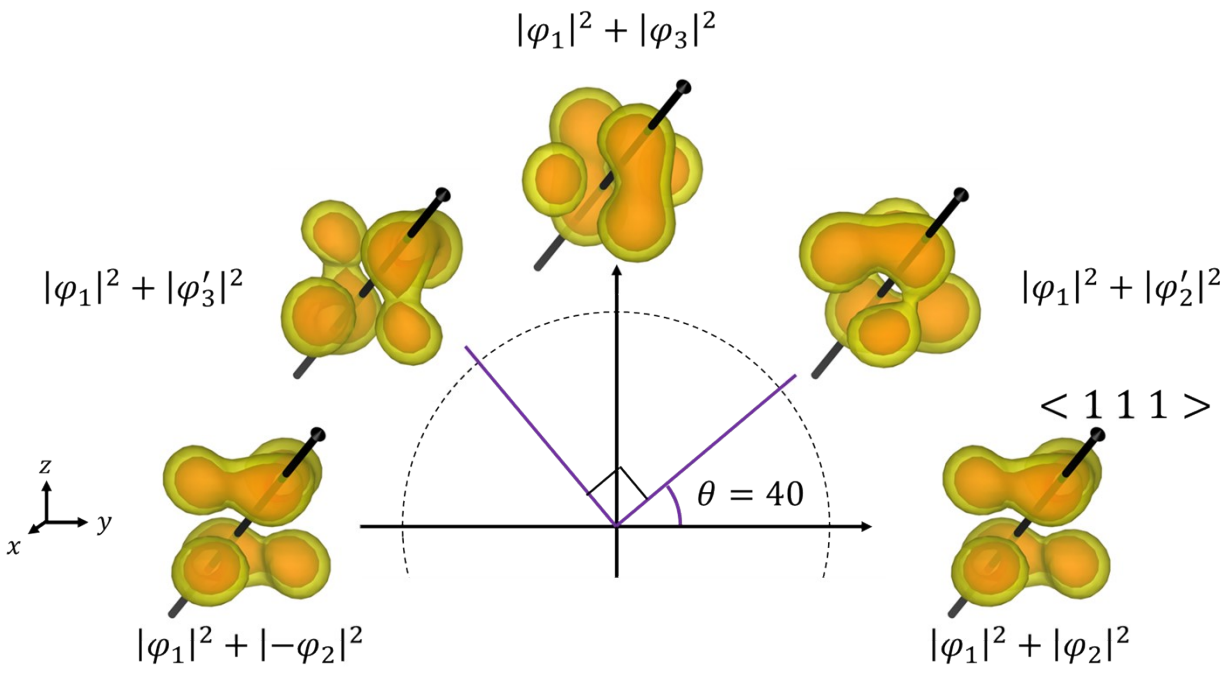

Fig. S3.

Simulated VEDs with $\theta = 0$ and $\theta = 40$. Simulated VEDs with $\theta > 180$ are omitted because these are the same as those from 0 to 180.

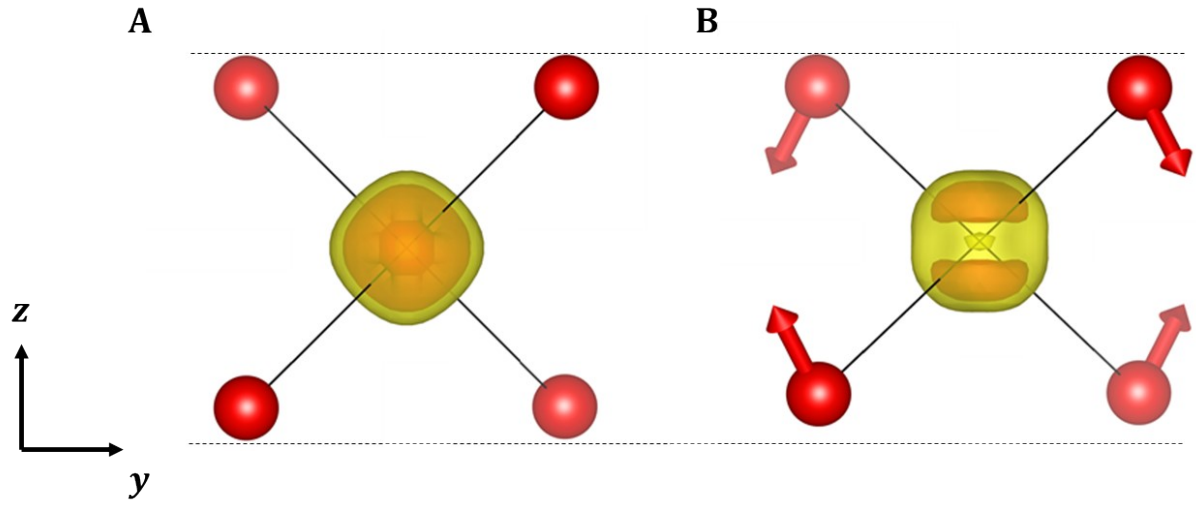

Fig. S4.

FeO_4 tetrahedron and VED in the (**A**) cubic phase and (**B**) high-temperature tetragonal phase. The isosurface levels are $8.0 e/Å^3$ (yellow) and $10.0 e/Å^3$ (red). The size of VED is represented twice as large. The red arrows in (**B**) indicate the displacement direction on O.

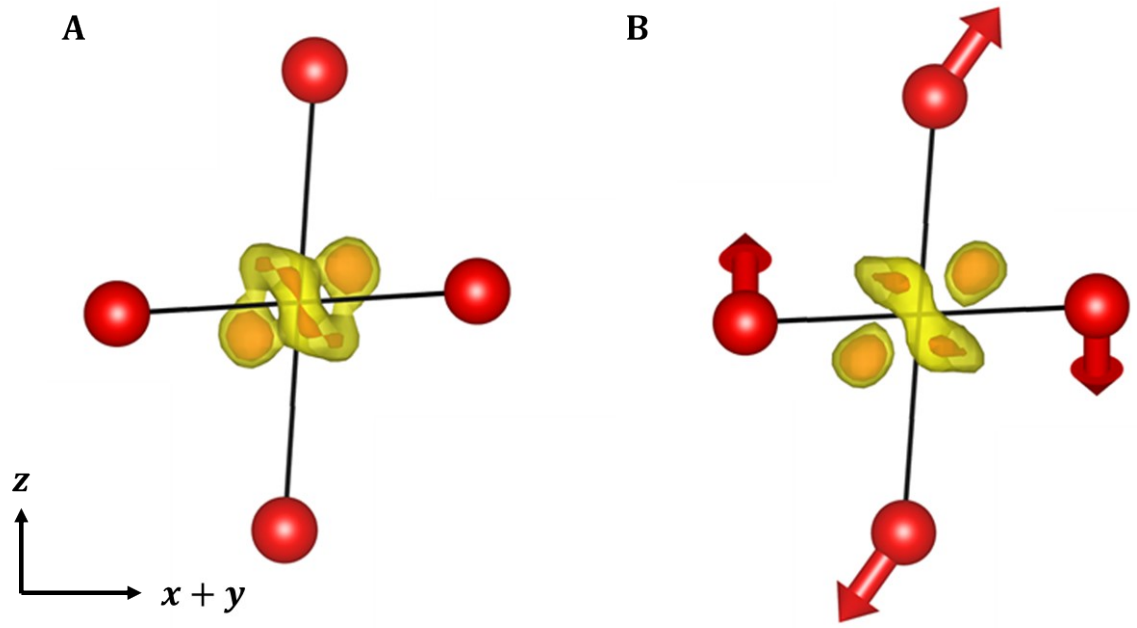

Fig. S5.

VO_6 octahedron and VED in the (**A**) cubic phase and (**B**) high-temperature tetragonal phase. The isosurface levels are $4.5 e/Å^3$ (yellow) and $5.3 e/Å^3$ (red) in (**A**), $3.8 e/Å^3$ (yellow) and $4.6 e/Å^3$ (red) in (**B**). The size of VED is represented twice as large. The red arrows in (**B**) indicate the displacement direction on O.

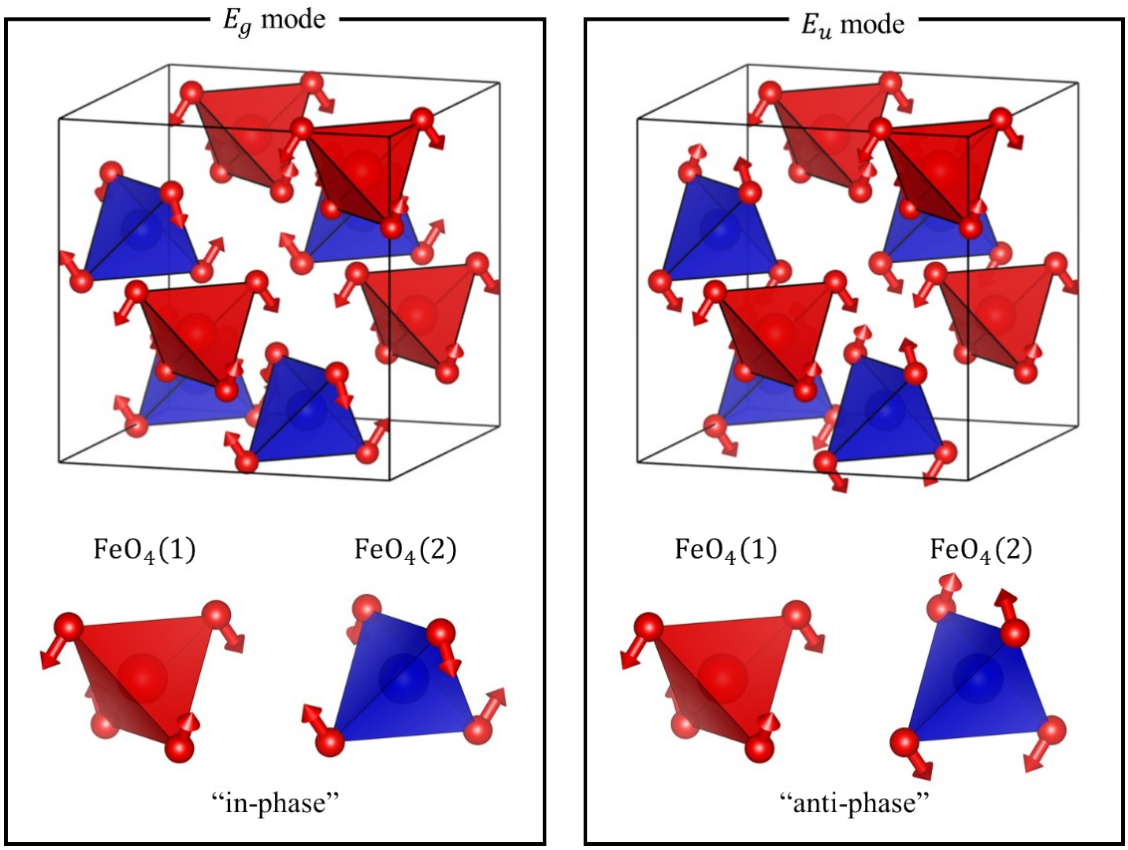

Fig. S6.

Schematic of the E_g and E_u phonon modes in FeV_2O_4. Only FeO_4 tetrahedrons are displayed.

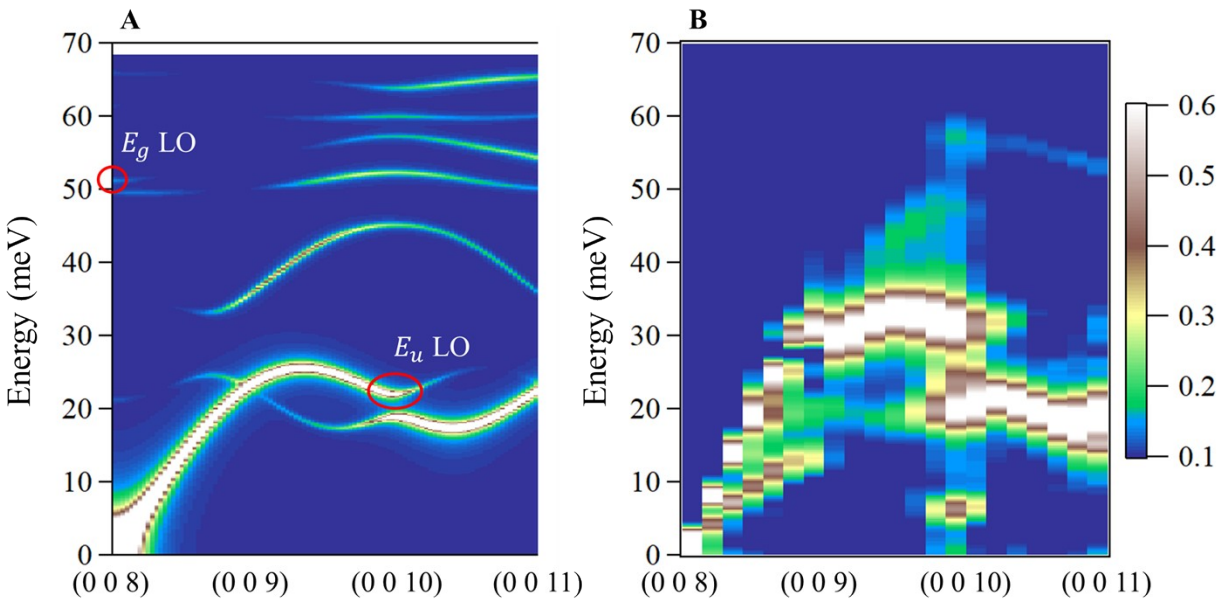

Fig. S7.

(**A**) 2D color plot of the energy spectra obtained from the first-principles calculations of phonon in the [0 0 1] direction from (0 0 8) in reciprocal space. (**B**) 2D color plot of the energy spectra obtained from IXS experiments at 300 K in the [0 0 1] direction from (0 0 8) in reciprocal space.

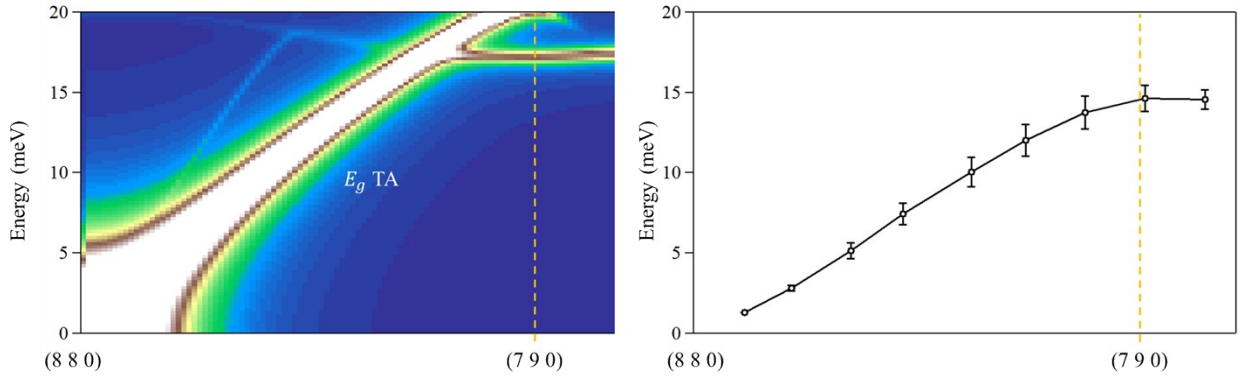

Fig. S8.

(**A**) 2D color plot of the energy spectra obtained from the first-principles calculations of phonon in the [-1 1 0] direction from (8 8 0) in reciprocal space. (**B**) Dispersion obtained from IXS experiments at 300 K in the [-1 1 0] direction from (8 8 0) in reciprocal space. The phonon energy linewidth is used as an error bar of each data.

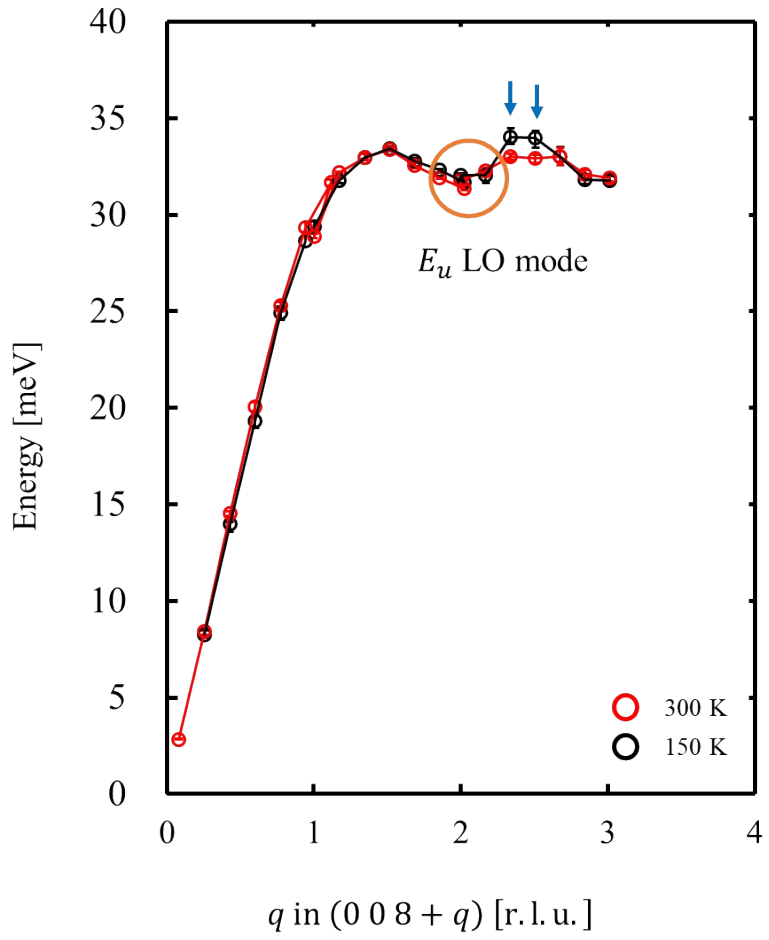

Fig. S9.

Phonon dispersions of E_u LO mode at 300 K and 150 K. The difference in the data points pointed by the blue arrows is an analytic problem caused by the weak intensity of the phonon peak and is not important.

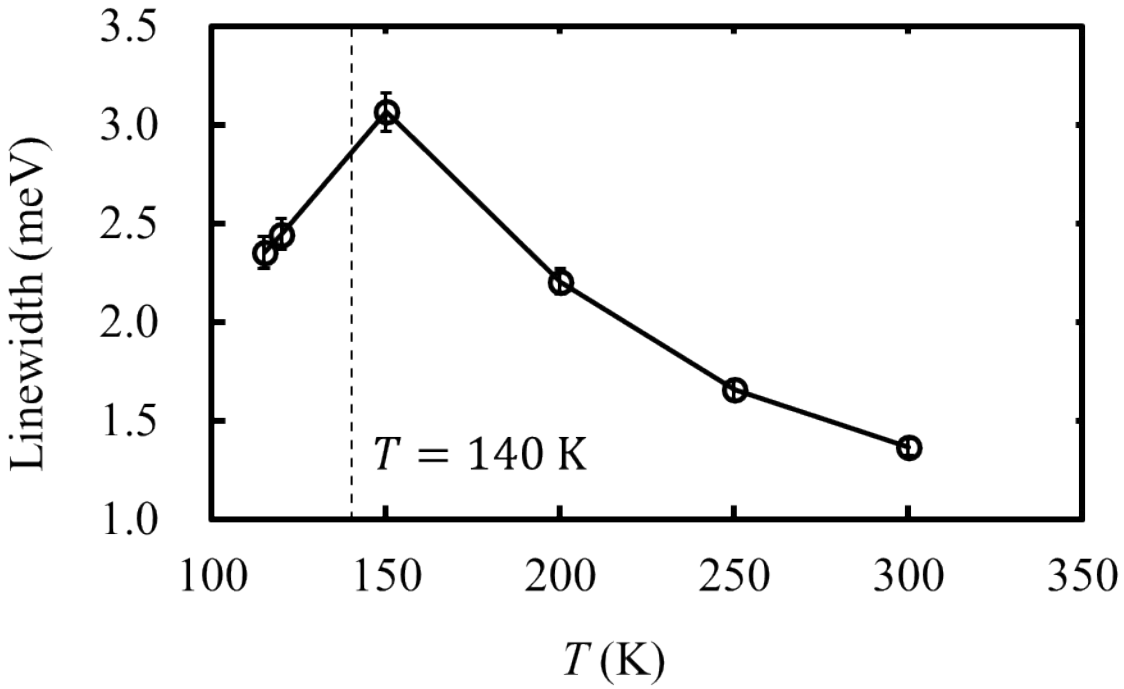

Fig. S10.

The temperature dependence of the phonon energy linewidth at Q = (7.54 8.45 − 0.03).

Table S1.

Crystallographic data of the cubic phase in FeV_2O_4.

Temperature (K)	160
Wavelength (Å)	0.309501
Crystal dimension (μm^3)	40 × 40 × 10
Space group	$Fd\bar{3}m$
a (Å)	8.4453(7)
V (Å^3)	602.3(2)
Z	8
F (000)	832
$(\sin\theta/\lambda)_{Max}$ (Å^{-1})	1.79
$N_{Total,obs}$	36870
$N_{Unique,obs}$	787
Average redundancy	46.8
Completeness	0.990
High-angle analysis [$0.83\ \text{Å}^{-1} \leq \sin\theta/\lambda \leq 1.79\ \text{Å}^{-1}$] ($N_{Parameters} = 7$)	
R_1 [# of reflections]	0.0204 [651]
R_1 ($I > 3\sigma$) [# of reflections]	0.0132 [586]
GOF [# of reflections]	1.17 [651]
Normal analysis [$0\ \text{Å}^{-1} \leq \sin\theta/\lambda \leq 1.79\ \text{Å}^{-1}$] ($N_{Parameters} = 0$)	
R_1 [# of reflections]	0.0261 [742]
R_1 ($I > 3\sigma$) [# of reflections]	0.0170 [676]
GOF [# of reflections]	1.46 [742]

Table S2.

Structural parameters of the cubic phase in FeV_2O_4.

Atom	Wyckoff position	$x = y = z$	$U_{11} = U_{22} = U_{33}\ (\text{Å}^2)$	$U_{12} = U_{23} = U_{13}\ (\text{Å}^2)$
Fe	8*a*	$1/8$	$0.00392(1)$	0
V	16*d*	$1/2$	$0.00266(1)$	$-0.00013(1)$
O	32e	$0.73874(2)$	$0.00416(2)$	$-0.00049(3)$

Table S3.

Crystallographic data of the high-temperature tetragonal phase in FeV_2O_4.

Temperature (K)	120
Wavelength (Å)	0.521520
Crystal dimension (μm^3)	40 × 40 × 10
Space group	$I4_1/amd$
a (Å)	6.0159(2)
c (Å)	8.3513(1)
V (Å^3)	302.25(2)
Z	4
F (000)	416
$(\sin\theta/\lambda)_{Max}$ (Å^{-1})	1.66
$N_{Total,obs}$	27233
$N_{Unique,obs}$	1546
Average redundancy	17.6
Completeness	0.982
High-angle analysis [$0.83\ \text{Å}^{-1} \leq \sin\theta/\lambda \leq 1.66\ \text{Å}^{-1}$] ($N_{Parameters}$ = 12)	
R_1 [# of reflections]	0.0230 [1272]
R_1 ($I > 3\sigma$) [# of reflections]	0.0202 [959]
GOF [# of reflections]	0.96 [1272]
Normal analysis [$0\ \text{Å}^{-1} \leq \sin\theta/\lambda \leq 1.66\ \text{Å}^{-1}$] ($N_{Parameters}$ = 0)	
R_1 [# of reflections]	0.0235 [1478]
R_1 ($I > 3\sigma$) [# of reflections]	0.0190 [1152]
GOF [# of reflections]	1.03 [1478]

Table S4.

Structural parameters of the high-temperature tetragonal phase in FeV_2O_4. The isotropic atomic displacement parameter is used at the Fe site for the CDFS method.

Atom	Wyckoff position	*x*	*y*	*z*
Fe	4*a*	0	3/4	1/8
V	8*d*	0	0	1/2
O	16h	0	0.47513(14)	0.25870(9)

Atom	U_{11} (Å^2)	U_{22} (Å^2)	U_{33} (Å^2)	U_{12} (Å^2)	U_{13} (Å^2)	U_{23} (Å^2)
Fe	0.00411(2)	0	0	0	0	0
V	0.00311(4)	0.00281(4)	0.00319(4)	0	0	0.00010(2)
O	0.00535(14)	0.00442(14)	0.00425(12)	0	0	0.00051(6)

References

1. R. H. Blessing, Data Reduction and Error Analysis for Accurate Single Crystal Diffraction Intensities. *Crystallogr. Rev.* 1987, **1**, 3–58.
2. V. Petříček, M. Dušek, L. Palatinus, Crystallographic Comuting System JANA2006: General features. *Z. Kristallogr. -Cryst. Mater.* 2014, **229**, 345–352.
3. K. Momma, F. Izumi, VESTA 3 for three-dimensional visualization of crystal, volumetric and morphology data. *J. Appl. Crystallogr.* 2011, **44**, 1272–1276.
4. X. Gonze, B. Amadon, G. Antonius, F. Arnardi, L. Baguet, J. M. Beuken, J. Bieder, F. Bottin, J. Bouchet, E. Bousquet, N. Brouwer, F. Bruneval, G. Brunin, T. Cavignac, J. B. Charraud, W. Chen, M. Côté, S. Cottenier, J. Denier, G. Geneste, P. Ghosez, M. Giantomassi, Y. Gillet, O. Gingras, D. R. Hamann, G. Hautier, X. He, N. Helbig, N. Holzwarth, Y. Jia, F. Jollet, W. Lafargue-Dit-Hauret, K. Lejaeghere, M. A. L. Marques, A. Martin, C. Martins, H. P. C. Miranda, F. Naccarato, K. Persson, G. Petretto, V. Planes, Y. Pouillon, S. Prokhorenko, F. Ricci, G. M. Rignanese, A. H. Romero, M. M. Schmitt, M. Torrent, M. J. van Setten, B. V. Troeye, M. J. Verstraete, G. Zérah, J. W. Zwanziger, The ABINIT project: Impact, environment and recent developments. *Comput. Phys. Commun.* 2020, **248**, 107042.
5. J. P. Perdew, Y. Wang, Accurate and simple analytic representation of the electron–gas correlation energy. *Phys. Rev. B*, 1992, **45**, 13244.
6. N. A. W. Holzwarth, A. R. Tackett, G. E. Matthews, A Projector Augmented Wave (PAW) code for electronic structure calculations. Part I: atompaw for generating atom-centered functions. *Comput. Phys. Commun.*, 2001, **135**, 329–347.
7. A. I. Liechtenstein, V. I. Anisimov, J. Zaanen, Density-functional theory and strong interactions: Orbital ordering in Mott–Hubbard insulators. *Phys. Rev. B*, 1995, **52**, R5467.
8. K. Wakiya, T. Onimaru, S. Tsutsui, T. Hasegawa, K. T. Matsumoto, N. Nagasawa, A. Q. R. Baron, N. Ogita, M. Udagawa, T. Takabatake, Low-energy optical phonon modes in the caged compound $LaRu_2Zn_{20}$. *Phys. Rev. B* **93**, 064105 (2016).
9. Y. Luan, Ph.D. *thesis*, University of Tennessee, 2011.